INTERNATIONAL JOURNAL OF
NUMERICAL ANALYSIS AND MODELING
Volume 17, Number 2, Pages 236–253

PROVABLY SIZE-GUARANTEED MESH GENERATION WITH SUPERCONVERGENCE

XIANGRONG LI, NAN QI*, WEIWEI ZHANG, AND YUFENG NIE

Abstract. The mesh conditions of high-quality grids generated by bubble placement method (BPM) and their superconvergence properties are studied in this paper. A mesh condition that for each pair of adjacent triangles, the lengths of any two oppsite edges differ only by a high order of the parameter h is derived. Furthermore, superconvergence estimations are analyzed on both linear and quadratic finite elements for elliptic boundary value problems under the above mesh condition. In particular, the mesh condition is found to be applicable to many known superconvergence estimations under different types of equations. Finally, numerical examples are presented to demonstate the superconvergence properties on BPM-based grids.

Key words. Bubble placement method, mesh condition, superconvergence estimation.

1. Introduction

Superconvergence of finite element solutions to partial differential equations has been studied intensively for many decades [1, 2, 3, 6]. It is shown to be an important tool to develop high-performance finite elements. The superconvergence property can significantly improve the accuracy of finite element solution and its derivatives with few extra calculation and storage. And it is mainly used to construct a posteriori error indicator [3].

The existing research work basically follows two approaches. One is to find the super-close point of finite element interpolation approximation, and then use the interpolation weak estimation to obtain the superconvergence properties of finite element solution and its derivatives [4, 5]. Another is to obtain superconvergence properties by various post-processing techniques, including weighted averaging, local L^2-projection, extrapolation, and gradient recovery methods. In particular, gradient recovery methods have achieved great success in numerical simulations in engineering problems, such as the popular superconvergent patch recovery (SPR) method [6, 7, 8] and the polynomial preserving gradient recovery (PPR) method [24].

However, in early superconvergence theory, specially structured grids were normally required, such as the strongly regular grids composed of equilateral triangles [9], which brought a great difficulty to mesh generation techniques. Thus a consensus was hardly reached between theory of superconvergence and mesh generation.

Recently, several studies have striven to relieve this issue. From one hand, superconvergence theory was well developed, though under assumed mesh conditions. In particular, Bank and Xu [10, 11] studied superconvergence on mildly structured grids where most pairs of elements form an 'approximate parallelogram'. They also

Received by the editors August 30, 2019.
2000 *Mathematics Subject Classification.* 65N50, 65N60, 65N15.
*Corresponding author.

proved that linear finite element solution is superclose to its linear interpolant of exact solution. From this work, Xu and Zhang [12] established the superconvergence estimations for several post-processing techniques. Further, Huang and Xu investigated superconvergence properties of quadratic triangular element on mildly structured grids [9]. From the other hand, superconvergence phenomena have existed in several mesh generation algorithms. For example, the centroidal Voronoi tessellation (CVT)-based methods have been successfully applied to develop high-quality grids [13]. However, its superconvergence estimations from some certain mesh conditions were not clearly provided [14].

In recent years, the so called bubble placement method (BPM) has been systematically studied by Nie et. al. [15, 16, 17]. The advantage of BPM is to generate high-quality grids on many complexly bounded 2D and 3D domains, and BPM can be easily used in adaptive finite element method and anisotropic problems [18, 19, 20, 21, 22, 30]. In addition, due to the natural parallelism of BPM, computational efficiency has been improved greatly to solve large-scale problems [23]. Yet, superconvergence on BPM-based grids has not been fully explored. The goal of this paper is to analyze a mesh condition on BPM-based grids, such that superconvergence results can be obtained both theoretically and numerically.

In this paper, we will carefully investigate the superconvergence properties on BPM-based grids. Our work is mainly composed of two parts: in the first part, a mesh condition associated with element edge length and desired length is derived for BPM-based grids; the second part presents two superconvergence results for linear and quadratic finite elements, respectively. These superconvergence results can be used to construct posteriori error estimates under gradient recovery operators.

The rest of this paper is organized as follows. Section 2 gives the derivation of mesh conditions for BPM-based grids. Superconvergence estimations on linear and quadratic finite elements are analyzed in Section 3. Numerical experiments on elliptic boundary value problem with some typical computational domains are given in Section 4 and further discussed in Section 5. Conclusions and future works are summarized in Section 6.

2. Mesh conditions

2.1. BPM. Bubble placement method was originally inspired by the idea of bubble meshing [25, 26] and the principle of molecular dynamics. The computational domain is regarded as a force field with viscosity, and bubbles are distributed in this domain. Each bubble is driven by interaction forces from its adjacent bubbles, expressed as [27]:

$$f(w) = \begin{cases} k_0\left(1.25w^3 - 2.375w^2 + 1.125\right) & 0 \le w \le 1.5 \\ 0 & 1.5 < w. \end{cases} \tag{1}$$

The output of bubble centers are denoted as nodes in the computational domain, where $w = \frac{l_{ij}}{\bar{l_{ij}}}$, l_{ij} is the actual distance between bubble i and bubble j, $\bar{l_{ij}}$ is the user-defined distance. The motion of each bubble satisfies the Newton's second law of motion. BPM can be mainly divided into 3 steps: initialization, dynamic simulation, bubble insertion and deletion operations. And BPM is regarded to be controlled by two nested loops, which is schematically illustrated in Fig. 1.

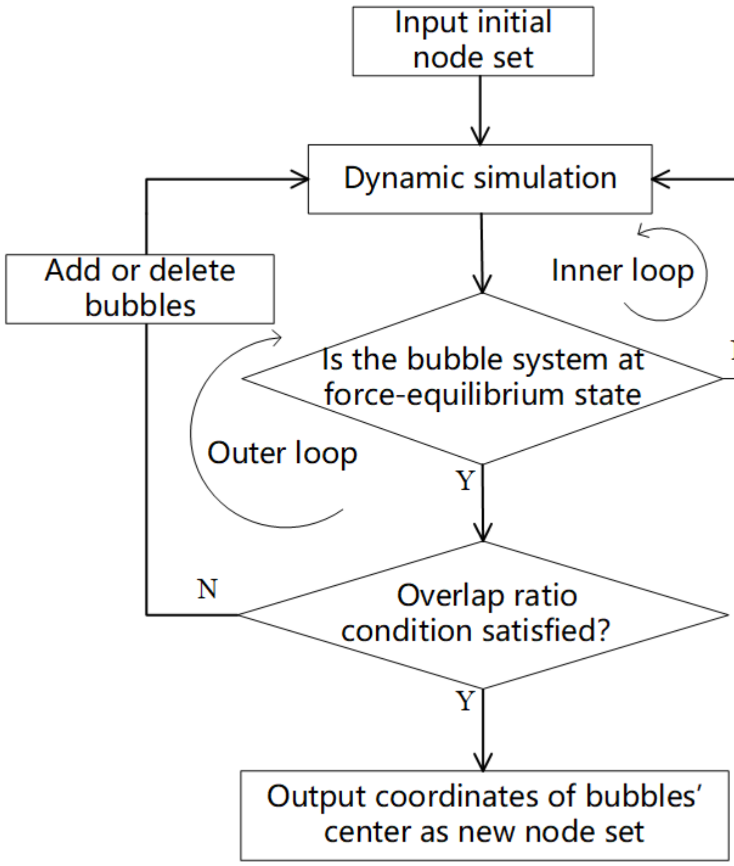

FIGURE 1. The flowchart of BPM.

The inner loop (dynamic simulation) ensures a good bubble distribution by balancing forces and the outer loop (insertion and deletion operations) controls the bubble number such that adjacent bubbles can be as tangent to each other as possible at force-equilibrium state. They both work together to get a closely-packed configuration of bubbles, so that a well-shaped and size-guaranteed Delaunay triangulation can be created by appropriately connecting the bubble centers.

2.1.1. Inner loop. In the inner loop, the motion of a bubble is analogous to a damped vibrator. In the initial state, a potential energy exists between bubbles, which partly converses to kinetic energy during simulation. The motion of the bubble system also leads to energy loss due to the damping force. The potential energy of the bubble system reaches its minimum at force-equilibrium state, and at this moment the resultant force exerting on each interior bubble vanishes.

It is worthwhile to note that for any interior bubble at force-equilibrium state, the applied forces from its adjacent bubbles are of same magnitude and sign. As illustrated in Fig. 2, in an 1D case, for any interior bubble k, if it overlaps with its left adjacent bubble $k-1$, there will be a repulsive force $f_{(k,k-1)}$ between bubble k and bubble $k-1$. At force-equilibrium state, as the resultant external force of

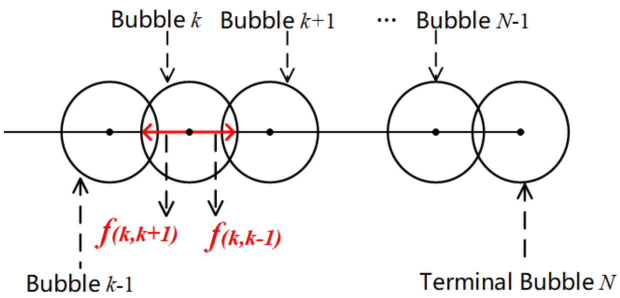

FIGURE 2. Force-equilibrium state in one-dimension. For bubble k, there is a repulsive force $f_{(k.k-1)}$ from bubble $k-1$. When system reaches an equilibrium state, resultant external force of bubble k is zero. Therefore, $f_{(k.k+1)}$ and $f_{(k.k-1)}$ must be same in magnitude and sign.

bubble k approaches to zero, there must exist a force in same magnitude and same sign ($'+'$ for repulsion and $'-'$ for attraction) from the right adjacent bubble $k+1$. By analogy, the application of forces on each interior bubble satisfy the same rule until the terminal bubble (note the terminal bubble is fixed).

Let us now define a bubble fusion degree $C_{ij} = \frac{\bar{l}_{ij} - l_{ij}}{l_{ij}} = 1 - w$, which characterizes the relative overlapping/disjoint degree of bubble i and bubble j. It is easy to derive the following relationship,

$$
\begin{cases} C_{ij} > 0 \Rightarrow \overline{l_{ij}} > l_{ij}, \text{bubble } i \text{ overlaps with bubble } j, \\ C_{ij} = 0 \Rightarrow \overline{l_{ij}} = l_{ij}, \text{bubble } i \text{ is tangent to bubble } j, \\ C_{ij} < 0 \Rightarrow \overline{l_{ij}} < l_{ij}, \text{bubble } i \text{ is disjoint from bubble } j. \end{cases} \tag{2}
$$

Note that if the inter-force between two adjacent bubbles are the same in magnitude and sign, the variable w becomes a constant due to the monotonically attractive/repulsive force definition in Eq. (1). Thus the bubble fusion degree of any two adjacent bubbles is also a constant. It is essential to address that the bubble fusion degree, for any directions in 2D cases, is a constant such as the one in the 1D case. The corresponding bubble distribution is called force-equilibrium distribution in later sections.

To illustrate, we execute BPM algorithm with an assigned size function as $d(x, y) = h = 0.1$ on an unit circle region. As shown in Fig. 3, with an increasing time step T, the initial bubble distribution gradually tends to the force-equilibrium state. Meanwhile, it can be seen that the value of C_{ij} approaches towards a constant of 0.28.

2.1.2. Outer loop. Let

$$
\epsilon^N = \max_{i,j \in \Gamma_N} |C_{ij}|, \tag{3}
$$

where N is the total number of bubbles in the current loop, and Γ_N denotes the bubble set at force-equilibrium state with bubble number N. Outer loop controls bubbles' number by an overlapping ratio[16], i.e., deleting bubbles with too large overlapping ratio, and adding new neighboring ones to bubbles with too small

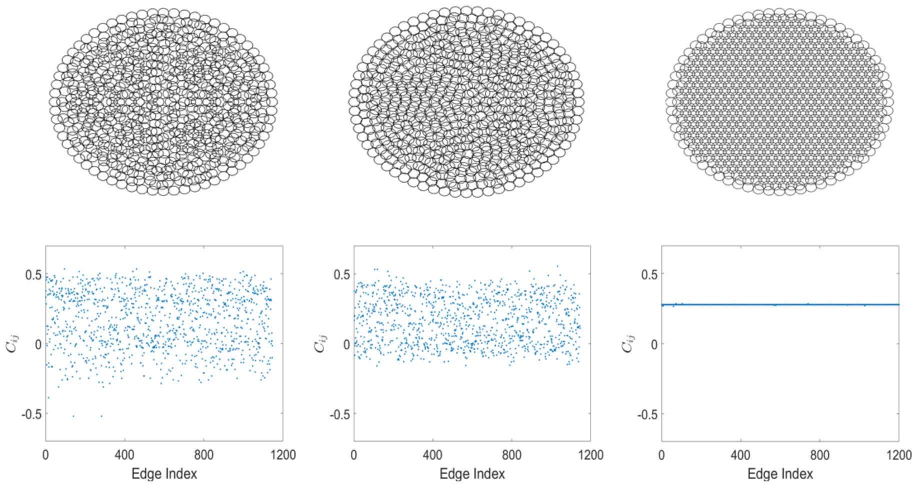

(A) T=0 (B) T=100 (C) T=200

FIGURE 3. The bubble distributions and the corresponding values of C_{ij} at different time steps.

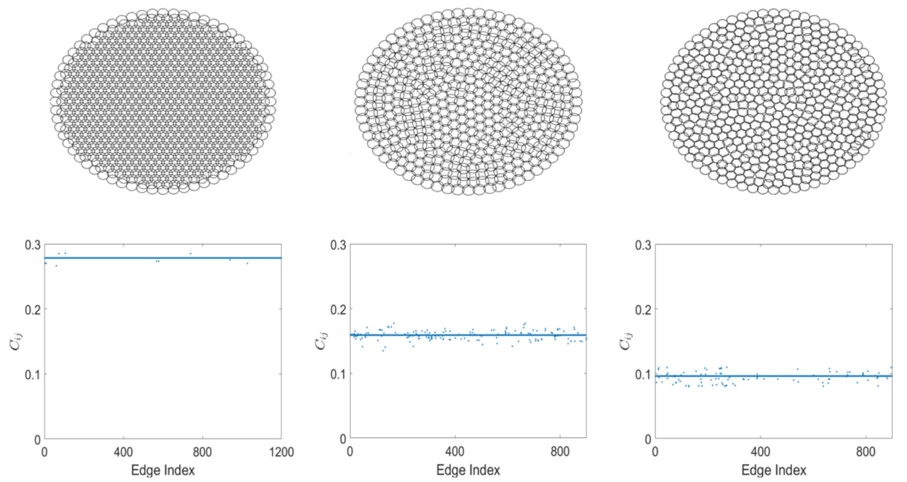

(A) $\epsilon^N = 0.317, N = 606$ (B) $\epsilon^N = 0.186, N = 488$ (C) $\epsilon^N = 0.112, N = 472$

FIGURE 4. The bubble distributions under addition/deletion operations and the corresponding values of C_{ij}.

overlapping ratio. If ϵ^N no longer reduces, the whole iterative process/the outer loop terminates.

For the same circle region in 2.1.1, Fig. 4 shows the bubble distributions with different total number of bubbles under addition/deletion operations. It can be seen that bubbles tend to become more tangent/with smaller overlaps, indicating that the actual distance between two adjacent bubbles become closer to their assigned

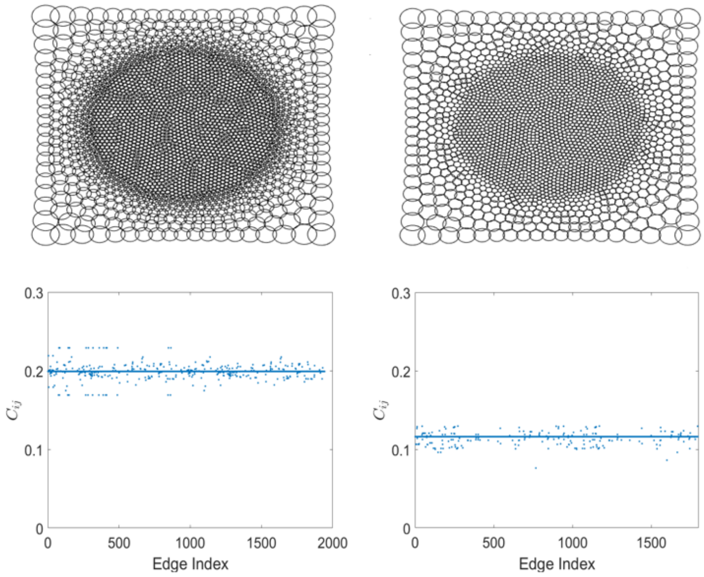

(A) $\epsilon^N = 0.236, N = 953$ (B) $\epsilon^N = 0.128, N = 862$

FIGURE 5. The bubble distributions and their corresponding values of C_{ij} for a non-uniform square example.

distance. Meanwhile, we can clearly see that values of C_{ij} and ϵ^N both decrease, implying that operations of adding or deleting bubbles are effective.

In summary, BPM can be interpreted mathematically as: to find a bubble set $\Gamma_{\bar{N}}$, such that

$$\Gamma_{\bar{N}} = \left\{ \Gamma_N : \min_N \left\{ \max_{i,j\in\Gamma_N} |C_{ij}| \right\} \right\}. \tag{4}$$

Remark 2.1. *The properties of inner loop and outer loop described above are also suitable for non-uniform cases. These are valid under certain continuity conditions, e.g., the Lipschitz continuity condition. And the Lipschitz constant is relevant to the dividing point in the piecewise inter-force function in Eq. (1)(e.g. 1.5 in this paper). We note that this continuity is local in BPM-based grids, which can be elaborated in a shock wave example, shown in Fig.6 of* [19]. *Herein, we also provide a non-uniform example by executing BPM algorithm on a square region* $[-3, 3] \times [-3, 3]$, *under a given size function*

$$d(x, y) = \begin{cases} 0.1 & \sqrt{x^2 + y^2} < 2, \\ 0.2 \times \left| \sqrt{x^2 + y^2} - 2 \right| + 0.1 & \sqrt{x^2 + y^2} \geq 2. \end{cases} \tag{5}$$

Numerical results are given in Fig. 5, where $\epsilon^N = 0.236$ *and* $\epsilon^N = 0.128$ *with total number of bubbles* $N = 953$ *and* $N = 862$, *respectively.*

2.2. Mesh conditions. It is aware that $\epsilon^{\bar{N}}$ can be used as a good indicator for maximum mesh relative error, so as to study mesh conditions of BPM-based grids.

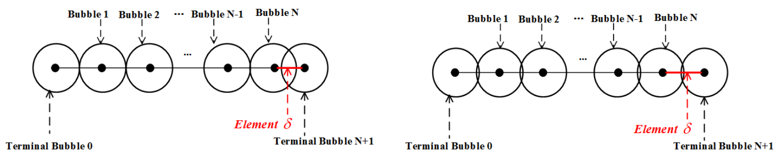

(A) before error averagely distributed

(B) after error averagely distributed

FIGURE 6. (A) The bubble distribution with N_t elements being ideally subdivided and (B) the bubble distribution at force-equilibrium state.

For a uniform case, i.e., its size function is a constant of h, then

$$\epsilon^N = \max_{i,j\in\Gamma_N} \left| \frac{h - l_{ij}}{h} \right|. \tag{6}$$

Let us denote an 'ideal subdivision' if the prescribed region can be precisely covered by equilateral triangles with assigned side size of h. For instance, an equilateral triangle region with side length of 1 can be divided into 25 equilateral triangles with length of 0.2, so that $\epsilon^{\bar{N}} = 0$. However, what we normally encounter is not an 'ideal subdivision'. So we have to look for a subdivision with $\bar{N}$ elements such that ϵ^N is minimized, and in general, its range can be easily estimated in advance.

Again, we start to illustrate from an 1D case. A domain with length L is required to be uniformly segmented into elements with size h. Let $N_\tau = \lfloor \frac{L}{h} \rfloor$ be the total number of uniform subdivision, and the length of the remaining segment after N_τ subdivisions is $l = L - N_\tau \cdot h$, and $l \in [0, h)$. This becomes an 'ideal subdivision' if $l = 0$. The element δ with length l introduces an error e_δ, in spite that all other elements are ideal (depicted in Fig. 6(A)). So the total error $e = \max\{e_\delta, 0\} = |h - l| = |h - (L - N_\tau \cdot h)| = |(N_\tau) \cdot h - L| = \mathcal{O}(h)$.

For a BPM-based grid, the bubble fusion degree of any two adjacent bubbles is a constant at force-equilibrium state, so the error of each element $|l_{ij} - h|$ is a constant, implying that the error e_δ is averaged over all elements (depicted in Fig. 6(B)). Thus

$$e = |h - l_{ij}| = \left| \frac{(N_\tau + 1) \cdot h - L}{N_\tau + 1} \right| \le \frac{h}{N_\tau + 1} \le \frac{h}{N_\tau} = \frac{h}{\lfloor \frac{L}{h} \rfloor} = O\left(h^2\right),$$

which presents a higher order of accurancy.

Analogously, as to a 2D case, a planar domain with area S is required to be uniformly segmented into equilateral triangles with side length of h. We know that the area of the equilateral triangle s_τ is $\frac{\sqrt{3}}{4}h^2 = O\left(h^2\right)$. However, the value of $N_\tau = \lfloor \frac{S}{s_\tau} \rfloor$ is not a good estimation since it ignores boundary effect. For instance, if we segment a circle with radius of 0.5 into equilateral triangles with side length of 0.3 starting from its center, there normally appears a ring-like area near the boundary that can not be precisely covered by equilateral triangles. Shown in Fig. 7, the number of uniform subdivision $N_\tau = 6$, therefore $\lfloor \frac{S}{s_\tau} \rfloor = 9$ over-estimates. We henceforth modify N_τ to be $\lfloor \frac{S}{s_\tau} \rfloor - n$, where n is a positive constant relating to the computational domain and given size function (e.g. $n = 3$ in the example of

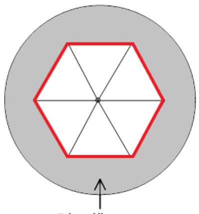

FIGURE 7. A 2D example of a circle segmented into equilateral triangles, where the ring-like area is highlighted in gray near the boundary, the uniform subdivision is bounded in red, so $N_\tau = 9 - 3 = 6$.

Fig. 7). Let $s = S - N_\tau \cdot s_\tau$ be the remaining area, by noting that $\lfloor \frac{S}{s_\tau} \rfloor > \frac{S}{s_\tau} - 1$ then we have

$$0 \leq s = S - (\lfloor \frac{S}{s_\tau} \rfloor - n) \cdot s_\tau = (S - \lfloor \frac{S}{s_\tau} \rfloor \cdot s_\tau) + ns_\tau < s_\tau + ns_\tau = (n+1)s_\tau.$$

Analogy to the 1D example, and we notice that $s_t = \mathcal{O}(h^2)$, so

$$0 \leq \lim_{h \to 0} \frac{e_s}{h^2} = \lim_{h \to 0} \frac{\left| \frac{S - N_\tau \cdot s_t}{N_\tau} \right|}{h^2} \leq \lim_{h \to 0} \frac{\frac{(n+1)s_\tau}{N_\tau}}{h^2} \leq \lim_{h \to 0} \frac{(n+1){s_\tau}^2}{(S - (n+1)s_\tau)h^2} = 0,$$

where e_s is the element error, and we note that $N_\tau \to N$, when $h \to 0$. As each edge shares the same order, then we obtain that the edge length error

$$e_h = |h - l_e| = \mathcal{O}(h^{1+\alpha}), \tag{7}$$

where α is an arbitrary positive constant, and l_e denotes the length of edge e, which is an equivalent denotation of the distance l_{ij} between bubble i and bubble j.

From Eqs. (6) and (7), we have $\epsilon^{\bar{N}} = \mathcal{O}(h^\alpha)$. Therefore, in BPM-based grids with $\Gamma^{\bar{N}}$,

$$|h - l_e| = \mathcal{O}(h^{1+\alpha}) \tag{8}$$

holds over all elements.

Remark 2.2. *For a non-uniform case, the error introduced by the remaining area s, instead of, averaged over all elements, distributed with some certain weights. One example of feasible weight candidates is presented as*

$$w_\tau = \frac{\bar{l}_{\tau_1} + \bar{l}_{\tau_2} + \bar{l}_{\tau_3}}{\sum\limits_k (\bar{l}_{k_1} + \bar{l}_{k_2} + \bar{l}_{k_3})}$$

where w_τ is the weight for the element τ, $\bar{l}_{\tau_i}, i = 1, 2, 3$ is its corresponding side lengths determined by the size function. Hence, the error of element τ is

$$e_\tau = |w_\tau(S - \sum_k s_k)|,$$

Similar to the analysis in uniform case, it follows that

$$\lim_{\bar{l}_{\tau_i} \to 0} \frac{e_\tau}{\bar{l}_{\tau_i}^{\,2}} = 0, (i = 1, 2, 3).$$

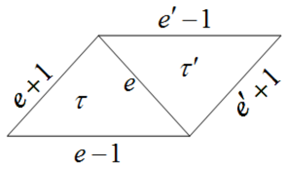

FIGURE 8. Notations in the patch Ω_e.

In particular, we know that in BPM-based grids, the size function satisfies locally continuous conditions. Therefore, we conclude that for any element τ,

$$|\bar{l}_{\tau_i} - l_{\tau_i}| = \mathcal{O}(\bar{l}_{\tau_i}^{\,1+\alpha})(\alpha > 0), (i = 1, 2, 3).$$

3. Superconvergence estimates on BPM-based grids

In the works of Bank, Xu, Zhang and Wu[10, 11, 12, 14, 29], they analyzed a series of superconvergence estimations on the basis of mildly structured grids, which requires that two adjacent triangles (sharing a common edge) form an $\mathcal{O}(h^{1+\alpha})$ ($\alpha > 0$) approximate parallelogram, i.e.

$$|l_{e+1} - l_{e'+1}| = \mathcal{O}(h^{1+\alpha}), \tag{9}$$

where l_e denotes the length of an interior edge e shared by two elements τ and τ'. l_{e+1} and $l_{e'+1}$ are the length of two opposite edges belonging to the patch $\Omega_e = \tau \cup \tau'$.

Yet, this key mesh condition has not been proved to be satisfied by any mesh generation techniques. However, from the derivation in Section 2, particularly from Eq.(8) and by using the triangle inequality, the mesh condition Eq. (9) can be easily obtained. In addition, some more rigorous mesh conditions can be also derived. For example, for neighboring edges, we have

$$|l_{e+1} - l_{e-1}| = \mathcal{O}(h^{1+\alpha}). \tag{10}$$

Henceforth, some useful superconvergence theories derived from the mesh condition Eq. (9) can be directly applied to BPM-based grids. And superconvergence estimations on linear and quadratic elements for Poisson problems are listed below, and more details are referred to [12, 14].

Lemma 3.1. *For a triangulation $\mathcal{T}_h$ generated by bubble-type mesh generation, for any $v_h \in {V_h}^k$*

$$\left|\int_\Omega \nabla(u - u_I)\nabla v_h\right| \lesssim h^{1+\min(\alpha,1/2)}\|v_h\|_{1,\Omega}, \tag{11}$$

$$\left|\int_\Omega \nabla(u - \Pi_Q u)\nabla v_h\right| \lesssim h^{2+\min(\alpha,1/2)}\|v_h\|_{1,\Omega}, \tag{12}$$

where ${V_h}^k = \{v_h : v_h \in H^1(\Omega), v_h|_\tau \in P_k(\tau)\}$, and u_I, $\prod_Q u$ are the linear and quadratic interpolants of u when $k = 1, 2$, respectively.

Let $\Omega \subset R^2$ be a bounded polygon with boundary $\partial\Omega$. Consider problem: Find $u \in V$ such that

$$a\,(u, v) = \int_\Omega \nabla u \nabla v\, dx = (f, v)\,, \forall v \in V, \tag{13}$$

where $(\cdot,\cdot)$ denotes inner product in the space $L^2(\Omega)$, and $V \subset H^1(\Omega)$. It is known that $a(\cdot,\cdot)$ is a bilinear form which satisfies the following conditions:

(1) (Continuity) There exists $C \geq 0$ such that
$$|a(u,v)| \leq C\|u\|_{1,\Omega}\|v\|_{1,\Omega},$$
for all $u, v \in V$.

(2) (Coerciveness) There exists $M > 0$ such that
$$a(v,v) \geq M\|v\|^2_{1,\Omega}, \forall v \in V.$$

Let ${V_h}^k$ be the conforming finite element space associated with triangulation $\mathcal{T}_h$, then the finite element solution $u_h \in {V_h}^k$ satisfies

$$a(u_h, v) = (f, v), \forall v \in {V_h}^k. \tag{14}$$

Theorem 3.2. *Assume that the solution of (13) satisfies $u \in H^3(\Omega) \cap W^2_\infty(\Omega)$, and u_h is the solution of (14). Let $u_I \in {V_h}^1$ and $\Pi_Q u \in {V_h}^2$ be the linear and quadratic interpolants of u, respectively. For a triangulation $\mathcal{T}_h$ derived from BPM-based grids, we have*

$$\|u_h - u_I\|_{1,\Omega} = \mathcal{O}(h^{1+\min(\alpha,1/2)}), \tag{15}$$

and

$$\|u_h - \Pi_Q u\|_{1,\Omega} = \mathcal{O}(h^{2+\min(\alpha,1/2)}). \tag{16}$$

Proof. Taking $v_h = u_h - u_I$ in (11), we have

$$\begin{aligned}
{\|u_h - u_I\|_{1,\Omega}}^2 &= a(u_h - u_I, u_h - u_I) = a(u - u_I, u_h - u_I) \\
&= \left|\int_\Omega \nabla(u - u_I)\nabla(u_h - u_I)\right| \\
&\lesssim h^{1+\min(\alpha,1/2)}\|u_h - u_I\|_{1,\Omega}.
\end{aligned}$$

So (15) is obtained by canceling $\|u_h - u_I\|_{1,\Omega}$ on both sides of the inequality. Similarly, by taking $v_h = u_h - \Pi_Q u$ in (12), (16) can be easily obtained. □

4. Numerical examples

In this section, some numerical examples are reported to validate Theorem 3.2, so as to illustrate the superconvergence property of BPM-based grids on solving Poisson equations. To the purpose of evaluating superconvergence performance, uniform segmentations with constant size functions are analyzed. The examples considered include both ideal subdivisions and non-ideal subdivisions.

In order to quantify the mesh quality, we first adopt a ratio between the radius of the largest inscribed circle (times two) and the smallest circumscribed circle [28] to define the quality of element τ as

$$q_\tau(l_{\tau_1}, l_{\tau_2}, l_{\tau_3}) = \frac{2r_{in}}{r_{out}} = \frac{(l_{\tau_2} + l_{\tau_3} - l_{\tau_1})(l_{\tau_3} + l_{\tau_1} - l_{\tau_2})(l_{\tau_1} + l_{\tau_2} - l_{\tau_3})}{l_{\tau_1} l_{\tau_2} l_{\tau_3}},$$

where l_{τ_1}, l_{τ_2}, l_{τ_3} are the computed side lengths of element τ. If an element is an equilateral triangle, then $q_\tau = 1$. We also define the average mesh quality over the whole computational domain as

$$Q_{avg} = \frac{1}{M}\sum_{\tau=1}^{M} q_\tau,$$

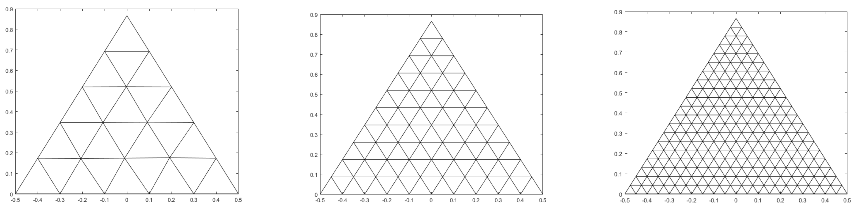

(A) $h = 0.2$ (B) $h = 0.1$ (C) $h = 0.05$

FIGURE 9. BPM-based grids on an equilateral triangle region with different h.

TABLE 1. Superconvergence results for an equilateral triangle region.

h	$\|u_h - u_I\|_{1,\Omega}$	order (k=1)	$\|u_h - \Pi_Q u\|_{1,\Omega}$	order (k=2)	Q_{avg}
0.2	1.81E-01		8.93E-03		0.9998
0.1	4.30E-02	2.08	1.14E-03	2.97	1.0000
0.05	1.05E-02	2.05	1.41E-04	3.02	1.0000
0.025	2.63E-03	2.01	1.78E-05	2.96	1.0000
0.0125	6.55E-04	2.01	2.30E-056	2.95	1.0000

where M represents the number of elements. The closer the value of Q_{avg} to 1, the higher mesh quality is, so that the more regular the grid is.

4.1. Example 1: An equilateral triangle region. The computational domain is an equilateral triangle with side length 1, and we solve Poisson equation on it with Dirichlet boundary conditions. The right-hand side f and the boundary conditions are chosen such that the exact solution is $u = \cos 2\pi x \sin 2\pi y$. The initial size $h = 0.2$, and it is reduced by half successively, the first three BPM-based grid configurations with $h = 0.2, 0.1, 0.05$, respectively, are shown in Fig. 9. It is seen that the nearly ideal subdivisions are generated for all four cases.

Table 1 presents some key superconvergence results, where u_I and $\Pi_Q u$ are the linear and quadratic interpolants of u, respectively. The superconvergence properties are observed as the order of $\|(u_I - u_h)\|_{1,\Omega}$ and $\|u_h - \Pi_Q u\|_{1,\Omega}$ are larger than 1 and 2, respectively. Note that when h is smaller than 0.2, the corresponding Q_{avg} can achieve to 1 to its four decimal digits. It may indicate a close relevance between the superconvergence property and the grid regularity, which is also stated in [9].

4.2. Example 2: A circle region. Given a unit circle region centered at origin, the size values are taken as 0.2, 0.1, 0.05, 0.025, 0.0125, respectively. BPM-based grids are selectively shown in Fig. 10. Choosing the exact solution $u = sinxsiny$, some calculated results are presented in Table 2. Obviously, there is superconvergence phenomenon on BPM-based grids and the results clearly indicate that $\|u_h - u_I\|_{1,\Omega}$ and $\|u_h - \Pi_Q u\|_{1,\Omega}$ are very close to $\mathcal{O}(h^{1.50})$ and $\mathcal{O}(h^{2.50})$. Although the convergence order is lower than Example 1, these results are still consistent with theoretic estimations (15) and (16).

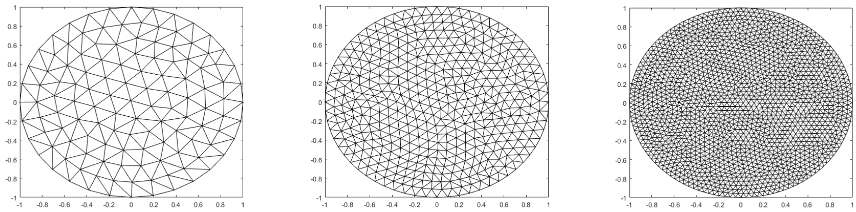

(A) $h = 0.2$ (B) $h = 0.1$ (C) $h = 0.05$

FIGURE 10. BPM-based grids on a circle region with different h.

TABLE 2. Superconvergence results for a circle region.

h	$\|u_h - u_I\|_{1,\Omega}$	order (k=1)	$\|u_h - \Pi_Q u\|_{1,\Omega}$	order (k=2)	Q_{avg}
0.2	1.09E-01		1.93E-02		0.9510
0.1	3.93E-02	1.47	3.53E-03	2.45	0.9635
0.05	1.36E-02	1.53	6.16E-04	2.52	0.9732
0.025	4.82E-03	1.50	1.09E-04	2.50	0.9702
0.0125	1.69E-03	1.51	1.96E-05	2.47	0.9753

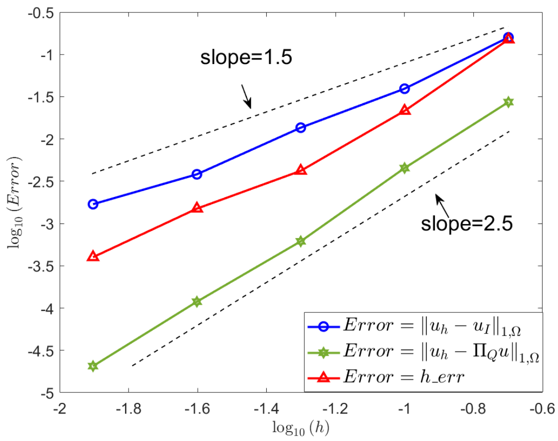

FIGURE 11. Comparison of different errors for a unit circle region. Dotted lines give reference slopes.

For a set of all edges $\mathcal{E}$, we denote $h_{err} = \frac{\sum |l_e - h|}{\#\mathcal{E}}$ as mean value of all edges' error. Fig. 11 plots the relationship between h_{err}, $\|u_h - u_I\|_{1,\Omega}$ and $\|u_h - \Pi_Q u\|_{1,\Omega}$, where logarithmic operations are applied on X and Y axes, so that the slope of $\log_{10}(Error)$ indicates the order of h. We can see that $\|(u_h - u_I)\|_{1,\Omega}$ and h_{err} have similar tendency, implying that the orders of errors in linear finite element solution and total edge length are consistent. Additionally, the slope of

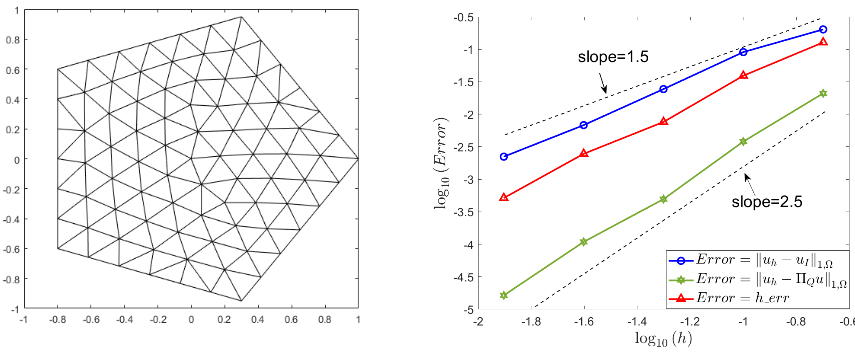

(A) BPM-based grids with $h = 0.2$ (B) Comparison of different errors

FIGURE 12. BPM-based grids on a regular pentagon region with $h = 0.2$ and comparison of different errors.

TABLE 3. Results for regular pentagon region.

h	$\|u_h - u_I\|_{1,\Omega}$	order (k=1)	$\|u_h - \Pi_Q u\|_{1,\Omega}$	order (k=2)	Q_{avg}
0.2	9.52E-02		9.37E-03		0.9582
0.1	3.34E-02	1.51	1.70E-03	2.46	0.9651
0.05	1.09E-02	1.62	2.77E-04	2.62	0.9608
0.025	3.74E-03	1.54	4.86E-05	2.51	0.9670
0.0125	1.25E-03	1.58	8.31E-06	2.55	0.9711

$\log_{10}(\|u_h - \Pi_Q u\|_{1,\Omega})$ is nearly one order higher than the one of $\|u_h - u_I\|_{1,\Omega}$, which is in line with the superconvergence estimation in Theorem 3.2.

4.3. Example 3: A regular pentagon region. Same procedure are followed except choosing the exact solution $u = e^{x+y}$ on a regular pentagon region. Table 3 shows again that $\|u_h - u_I\|_{1,\Omega} = \mathcal{O}\left(h^{1.55}\right)$ and $\|u_h - \Pi_Q u\|_{1,\Omega} = \mathcal{O}(h^{2.50})$, and the comparison are presented in Fig. 12(B), which may restates the rationality of Theorem 3.2.

5. Discussion

We have provided some typical numerical examples validating our theoretical results on many uniform BPM-based grids. And some special situations are discussed in details as follows.

5.1. The superconvergence estimations on domains with singularities. From above examples, we have mainly tested on convex domains since superconvergence estimation requires $u \in H^3(\Omega) \cap W^2_\infty(\Omega)$. In fact, many solutions may have singularities at corners. On account of this issue, Wu and Zhang [29] had deduced superconvergence estimation on domains with re-entrant corners for a Poisson

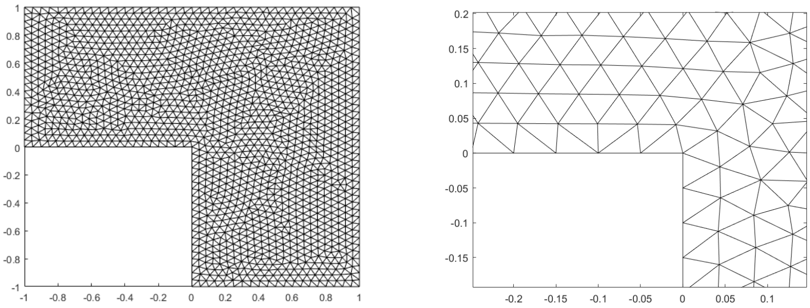

(A) (B)

FIGURE 13. (A) Mesh segmentation of an L-shape region with $h = 0.05$; (B) Local zoom in at the re-entrant corner.

TABLE 4. Results for four types of regions.

Domain	*mean*	*var*	$\max_{e\in\mathcal{E}} \lvert l_e - h\rvert$	$h_{err} = \frac{\sum \lvert l_e - h\rvert}{\#\mathcal{E}}$
Unit equilateral triangle	0.1000	7.0481e-14	4.6798e-07	1.6826e-07
Unit circle	0.0965	5.0513e-5	0.0184	0.0093
Regular pentagon	0.0955	7.3520e-5	0.0213	0.0087
L-shape	0.0946	2.0061e-4	0.0301	0.0120

Note: $Mean$ denotes the mean value of all edges' actual lengths, and var is their variance value. Let $\mathcal{E}$ be the set of edges, l_e the length of edge e, so h_{err} represents the mean value of all edges' errors.

equation on mildly structured grids as

$$\begin{cases} \|u_h - u_I\|_{1,\Omega} \lesssim N_d^{-\frac{1}{2}-\rho}, \\ \|u_h - \Pi_Q u\|_{1,\Omega} \lesssim N_d^{-1-\rho}, \end{cases} \tag{17}$$

where $\rho > 0$ is related to some mesh parameters, and N_d is the total number of degrees of freedom.

Based on (17), an L-shape region is selected to investigate the superconvergence properties on domains with singularities. Shown in Fig. 13, elements near the re-entrant corner are still well-shaped. The boundary conditions are chosen so that the true solution is $r^{2/3}\sin\frac{2}{3}\left(\theta + \frac{\pi}{2}\right)$ in polar coordinates. Fig. 14 compares the logarithm of errors in linear and quadratic solutions to the optimal convergence rates (-0.5 and -1), respectively. It is clear to deduce that $\|u_h - u_I\|_{1,\Omega}$ and $\|u_h - \Pi_Q\|_{1,\Omega}$ are both superconvergent, which is consistent with (17).

5.2. The superconvergence estimations modification caused by 'bad edges'. Numerically, we notice that the mesh condition (8) is hardly satisfied for all edges in BPM-based grids, i.e., there may exist few poor-shaped elements. Therefore, we reanalyze the above four types of computing regions with $h = 0.1$ aiming to

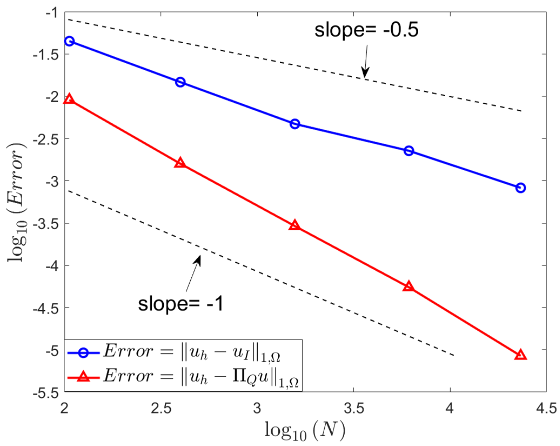

FIGURE 14. Comparison of different errors for a L-shaped domain. Dotted lines give reference slopes.

evaluate the performance of edges. Table 4 shows that the mean edge length are all very closed to $h = 0.1$.

However, compared with the mean edge errors h_{err}, the maximal edge errors $\max_{e\in\mathcal{E}} |l_e - h|$ are normally more than doubled, implying that edges with large errors (denoted as 'bad edges') are presented in computational domains. In fact, due to numerical errors, the bubble system reaches a particularly close force-equilibrium state, thus the bubble fusion degrees of a few bubbles are not precisely equal to a constant, leading to errors of 'bad edges' being in a reduced order.

However, the number of these bad edges is very small since our algorithm guarantees nearly zero resultant force for each bubble, which is also justified by the fact that the variance of edges length are extremely close to zero, so as the maximal and average edge errors, shown in Table 4.

Hence, to depict the errors caused by 'bad edges', we follow the arguments about 'bad edges' set considered in [12, 29] and modify mesh conditions in BPM-based grids accordingly. Denote $\mathcal{E} = \mathcal{E}_1 \oplus \mathcal{E}_2$ be the set of all edges belongs to triangulation $\mathcal{T}_h$, where $\mathcal{E}_1$ and $\mathcal{E}_2$ are 'good edges' and 'bad edges' sets, respectively, then the mesh condition is modified into

(1) For any edge $e \in \mathcal{E}_1$

$$|l_e - h| = \mathcal{O}\left(h^{1+\alpha}\right), \tag{18}$$

where α is a positive number.

(2) For any edge in $e \in \mathcal{E}_2$, $|l_e - h| = \mathcal{O}(h)$, and there exists a positive number σ such that

$$\sum_{e\in\mathcal{E}_2} (|\tau| + |\tau'|) = \mathcal{O}\left(h^{2\sigma}\right), \tag{19}$$

where τ and τ' are the two elements sharing edge e;

or

$$\sharp\mathcal{E}_2 \lesssim N^{-\sigma}, \tag{20}$$

where N is the total edge number.

For the two equivalent mesh conditions (19) and (20), they both require that the number of 'bad edges' are comparably small.

Accordingly, the superconvergence estimations need to be modified as follows:

$$\|u_h - u_I\|_{1,\Omega} = \mathcal{O}(h^{1+\min(\alpha,\sigma,1/2)}), \tag{21}$$

and

$$\|u_h - \Pi_Q u\|_{1,\Omega} = \mathcal{O}(h^{2+\min(\alpha,\sigma,1/2)}). \tag{22}$$

Note that there is merely a slight modification by adding the parameter σ deriving from mesh conditions (19) and (20). And particularly, superconvergence properties of our numerical experiments in Section 4 are still valid.

6. Conclusion

To conclude, many good properties of BPM algorithm have been detected in this paper. In the force-equilibrium state, inter-forces between two adjacent bubbles are the same, so that the bubble fusion degree appears constant for both uniform and non-uniform bubble distributions. From these analyses, mesh conditions based on edge errors are derived, which can be directly applied to many established superconvergence theories. These estimations take account of both linear and quadratic finite element solutions. Though simple two-dimensional Poisson equations are studied in our current preliminary superconvergence analysis on BPM-based grids, complex equations, e.g., general elliptic equations or other time-independent problems, need to be further considered.

It is for the first time that mesh conditions of BPM-based grids are theoretically derived and successfully applied to existing superconvergence estimations. Furthermore, we believe that our derivations can be easily applied to posterior error estimations and adaptive finite element methods in order to improve the accuracy of finite element solutions.

Acknowledgments

This research was supported by National Natural Science Foundation of China (No.11971386 and No.11501450), the Fundamental Research Funds for the Central Universities (No.3102017zy038 and No.2018HW012), and Natural Science Foundation of Shandong Province (No.ZR2019QA014).

References

[1] J. Douglas, T. Dupont, Superconvergence for galerkin methods for the two point boundary problem via local projections, Numerische Mathematik 21 (3) (1973) 270–278.
[2] N. Levine, Superconvergent recovery of the gradient from piecewise linear finite-element approximations, IMA Journal of Numerical Analysis 5 (4) (1985) 407–427.
[3] L. B. Wahlbin, Superconvergence in galerkin finite element methods, Lecture Notes in Mathematics 1605 (3) (1995) 269–285.
[4] R. Lin, Z. Zhang, Natural superconvergent points of triangular finite elements, Numerical Methods for Partial Differential Equations 20 (6) (2004) 864–906.

[5] W. Cao, Superconvergence of a quadratic finite element method on adaptively refined anisotropic meshes, International Journal of Numerical Analysis and Modeling 15 (1-2) (2018) 288–306.

[6] J. Zhu, O. Zienkiewicz, Superconvergence recovery technique and a posteriori error estimators, International Journal for Numerical Methods in Engineering 30 (7) (1990) 1321–1339.

[7] O. C. Zienkiewicz, J. Z. Zhu, The superconvergent patch recovery and a posteriori error estimates. part 1: The recovery technique, International Journal for Numerical Methods in Engineering 33 (7) (1992) 1331–1364.

[8] O. C. Zienkiewicz, J. Z. Zhu, The superconvergent patch recovery and a posteriori error estimates. part 2: Error estimates and adaptivity, International Journal for Numerical Methods in Engineering 33 (7) (1992) 1365–1382.

[9] Y. Huang, J. Xu, Superconvergence of quadratic finite elements on mildly structured grids, Mathematics of Computation 77 (263) (2008) 1253–1268.

[10] R. E. Bank, J. Xu, Asymptotically exact a posteriori error estimators, part i: Grids with superconvergence, SIAM Journal on Numerical Analysis 41 (6) (2003) 2294–2312.

[11] R. E. Bank, J. Xu, Asymptotically exact a posteriori error estimators, part ii: General unstructured grids, SIAM Journal on Numerical Analysis 41 (6) (2003) 2313–2332.

[12] J. Xu, Z. Zhang, Analysis of recovery type a posteriori error estimators for mildly structured grids, Mathematics of Computation 73 (247) (2003) 1139–1152.

[13] Q. Du, V. Faber, M. Gunzburger, Centroidal voronoi tessellations: Applications and algorithms, SIAM Review 41 (4) (1999) 637–676.

[14] Y. Huang, H. Qin, D. Wang, Centroidal voronoi tessellation-based finite element superconvergence, International Journal for Numerical Methods in Engineering 76 (12) (2008) 1819–1839.

[15] Y. Nie, W. Zhang, Y. Liu, L. Wang, A node placement method with high quality for mesh generation, IOP Conference Series: Materials Science and Engineering 10 (1) (2010) 012218.

[16] Y. Liu, Y. Nie, W. Zhang, L. Wang, Node placement method by bubble simulation and its application, Computer Modeling in Engineering and Sciences 55 (1) (2010) 89–109.

[17] N. Qi, Y. Nie, W. Zhang, Acceleration strategies based on an improved bubble packing method, Communications in Computational Physics 16 (1) (2014) 115–135.

[18] L. Cai, Y. Nie, W. Xie, W. Zhang, Numerical path integration method based on bubble grids for nonlinear dynamical systems, Applied Mathematical Modelling 37 (3) (2013) 1490–1501.

[19] W. Zhang, Y. Nie, L. Cai, N. Qi, An adaptive discretization of incompressible flow using node-based local meshes, Computer Modeling in Engineering & Sciences 102 (1) (2014) 55–81.

[20] W. Zhang, Y. Nie, Y. Gu, Adaptive finite element analysis of elliptic problems based on bubble-type local mesh generation, Journal of Computational and Applied Mathematics 280 (2015) 42–58.

[21] Y. Zhou, Y. Nie, W. Zhang, A modified bubble placement method and its application in solving elliptic problem with discontinuous coefficients adaptively, International Journal of Computer Mathematics 94 (6) (2016) 1268–1289.

[22] F. Wang, Y. Nie, W. Zhang, W. Guo, Npbs-based adaptive finite element method for static electromagnetic problems, Journal of Electromagnetic Waves and Applications 30 (15) (2016) 2020–2038.

[23] Y. Nie, W. Zhang, N. Qi, Y. Li, Parallel node placement method by bubble simulation, Computer Physics Communications 185 (3) (2014) 798–808.

[24] Z. Zhang, Polynomial preserving gradient recovery and a posteriori estimate for bilinear element on irregular quadrilaterals, International Journal of Numerical Analysis & Modeling 1 (1) (2004) 1–24.

[25] K. Shimada, J.-H. Liao, T. Itoh, Quadrilateral meshing with directionality control through the packing of square cells, International Meshing Roundtable (1998) 61–75.

[26] S. Yamakawa, K. Shimada, Quad-layer: Layered quadrilateral meshing of narrow two-dimensional domains by bubble packing and chordal axis transformation, Journal of Mechanical Design 124 (3) (2002) 564–573.

[27] K. Shimada, D. C. Gossard, Automatic triangular mesh generation of trimmed parametric surfaces for finite element analysis, Computer Aided Geometric Design 15 (3) (1998) 199–222.

[28] P. O. Persson, G. Strang, A simple mesh generator in matlab, SIAM Review 46 (2) (2004) 329–345.

[29] H. Wu, Z. Zhang, Can we have superconvergent gradient recovery under adaptive meshes?, SIAM Journal on Numerical Analysis 45 (4) (2007) 1701–1722.

[30] W. Guo, Y. Nie, W. Zhang, Anisotropic mesh adaptation method based on anisotropic bubble-type local mesh generation, International Journal of Numerical Analysis and Modeling 16 (5) (2019) 745–766.

Research Center for Computational Science, Northwestern Polytechnical University, Xi'an, Shannxi 710129, China.

E-mail: `xiangrong@mail.nwpu.edu.cn`

Institute of Marine Science & Technology, Shandong University, Qingdao, Shandong 250100, China.

E-mail: `Nan.Qi@sdu.edu.cn`

Research Center for Computational Science, Northwestern Polytechnical University, Xi'an, Shannxi 710129, China.

E-mail: `wwzhang@nwpu.edu.cn and yfnie@nwpu.edu.cn`